

Two physical regimes for the giant HII regions and giant molecular clouds in the Antennae Galaxies

J. Zaragoza-Cardiel^{1,2*}, J. Font^{1,2}, J. E. Beckman^{1,2,3}, B. García-Lorenzo^{1,2},
S. Erroz-Ferrer^{1,2}, and L. Gutiérrez⁴

¹*Instituto de Astrofísica de Canarias, C/ Vía Láctea s/n, 38205 La Laguna, Tenerife, Spain*

²*Department of Astrophysics, University of La Laguna, E-38200 La Laguna, Tenerife, Spain*

³*CSIC, 28006 Madrid, Spain*

⁴*Universidad Nacional Autónoma de México, Instituto de Astronomía, Ensenada, B. C., Mexico*

18 November 2014

ABSTRACT

We have combined observations of the Antennae galaxies from the radio interferometer ALMA (Atacama Large Millimeter/submillimeter Array) and from the optical interferometer GHαFaS (Galaxy H α Fabry-Perot System). The two sets of observations have comparable angular and spectral resolutions, enabling us to identify 142 giant molecular clouds (GMCs) and 303 HII regions. We have measured, and compared, their basic physical properties (radius, velocity dispersion, luminosity). For the HII regions, we find two physical regimes, one for masses $> 10^{5.4}M_{\odot}$ of ionized gas, where the gas density increases with gas mass, the other for masses $< 10^{5.4}M_{\odot}$ of ionized gas, where the gas density decreases with gas mass. For the GMCs, we find, in contrast to previous studies in other galaxies over a generally lower mass range of clouds, that the gas surface density increases with the radius, hinting at two regimes for these clouds if we consider both sources of data. We also find that the GMC mass function has a break at $10^{6.7}M_{\odot}$. Using the velocity dispersion measurements, we claim that the difference between the regimes is the nature of the dominant binding force. For the regions in the lower mass range, the dominant force is the external pressure, while in the higher mass range it is the internal gravity of the clouds. In the regime where gravity is dominant, the star formation rate, derived from the dust-corrected H α luminosity, increases super-linearly with the velocity dispersion, and the gas density increases with the gas mass.

Key words: galaxies: interactions – stars: formation – galaxies: starburst – galaxies: kinematics and dynamics – (ISM:) H ii regions – Nebulae, ISM: clouds

1 INTRODUCTION

Star formation takes place largely if not exclusively within molecular clouds (Klessen 2011; Scoville 2012). Studies of the statistical properties of molecular clouds help us to understand the processes involved in star formation, in both Galactic (Larson 1981; Heyer et al. 2009; Roman-Duval et al. 2010; Kauffmann et al. 2010) and extragalactic (Bolatto et al. 2008; Wei et al. 2012; Colombo et al. 2014) environments.

When the first massive stars form, the gas is heated and ionized leading to the formation of HII regions. This may cause the quenching of star formation via local gas stripping. However, if the original molecular clouds were sufficiently

massive, and thus strongly bound, the effects of this heating in disrupting the original cloud could be relatively moderate (Dale et al. 2012).

In addition, the detailed effects of galaxy interactions on star formation demand considerable further research (Bournaud 2011). Studying the properties of molecular clouds in galaxy interactions can reveal important clues about star formation and its role in the evolution of galaxies.

Larson (1981) studied the properties (luminosity/mass, size, and velocity dispersion) of 54 molecular clouds in the Galaxy, and found correlations between them. Nowadays, we call those correlations Larson’s laws, and we still do not know if they are universal. The correlation known as the third law is the mass size relation, which Larson found to follow $M \propto R^{1.9}$, i. e., the molecular gas surface density is approximately constant with size. The exponent

* E-mail: jzc@iac.es

in this relation has varied from study to study but always around 2 and considerably less than 3 (Roman-Duval et al. 2010; Lombardi et al. 2010; Kauffmann et al. 2010; Colombo et al. 2014). Colombo et al. (2014) found that the properties of the M51 giant molecular clouds (GMCs) apparently differ in the arms, the interarm regions and the circumnuclear zone. Statistical studies of molecular clouds can help us to study the star formation behaviour in different environments and on different scales. The study of the properties of GMCs in interacting galaxies is harder than in isolated galaxies due to the lack of suitable nearby examples. M51 is the closest pair of galaxies, however, the Antennae galaxies are the closest gas-rich major merger pair of galaxies. Thus, improving the spatial resolution and the sensitivity of observations of the Antennae could reveal new properties of the gas clouds.

Statistical studies of HII regions have been performed, but never compared explicitly with the equivalent properties of molecular clouds. There are, however, correlations between parameters (luminosity, size, and velocity dispersion) of HII regions which are equivalent to those for molecular clouds. The exponent Q in the $H\alpha$ luminosity-size relation, $L_{H\alpha} \propto R^Q$, has usually been found to have values of around 2 and significantly less than 3 (Terlevich & Melnick 1981; Gutiérrez et al. 2011). The luminosity-velocity dispersion relation has been proposed as a useful distance calibrator (Melnick et al. 1987; Chávez et al. 2014), but we still do not know what causes the width of the HII region velocity dispersions to change. Recent results are contradictory, pointing towards self-gravity (Zaragoza-Cardiel et al. 2013; Chávez et al. 2014) or towards the energy injected into the interstellar medium by the ongoing star formation (Moiseev et al. 2014).

The break in the luminosity function (Kennicutt, Edgar, & Hodge 1989; Bradley et al. 2006) at 38.6 dex has also been proposed as a distance calibrator. Defining the physical basis of the luminosity-velocity dispersion relation and the luminosity function break would clearly be important to validate them as distance calibrators.

The Antennae consist of a pair of galaxies in obvious interaction, which is classified as a luminous system in the infrared (LIRG, $L_{IR} = 10^{11}$; Sanders et al. (2003)). The two are in a fairly early stage of a merger process, so it is commonly accepted that, in the future, the system will develop into an ultra-luminous infrared galaxy (ULIRG). The luminosity is dominated by the infrared luminosity and the Antennae present off-nuclear obscured star forming regions (Mirabel et al. 1998; Wang et al. 2004). This makes the Antennae galaxies a particularly suitable system for understanding the role of star formation in the evolution of galaxies, as well as the formation of the off-nuclear peaks of star formation in galaxy mergers.

Previous authors have used the high resolution of the Hubble Space Telescope (*HST*) data to resolve super star clusters (SSC) in the Antennae (Anders et al. 2007; Whitmore et al. 2010), which gave rise to contradictory results about the presence of a turnover in the SSC luminosity function.

Recently, Wei et al. (2012) measured the physical parameters of molecular clouds in this interacting galaxy pair (also referenced as Arp 244) based on a combination

of observations of SMA (Submillimeter Array) and PdBI (Plateau de Bure Interferometer), yielding a synthesized angular resolution of $3.3\text{arcsec} \times 1.5\text{arcsec}$. They found that the mass function of the clouds identified in the CO(2-1) line emission shows a double peaked distribution, with a break at $\sim 10^{6.5} M_{\odot}$. They suggested that the clouds with masses below this value share the properties (essentially the dependence of mass and velocity dispersion on cloud radius) of the GMC's in normal star forming galaxies. The high mass cloud population is associated with sites of peak star formation. However, Ueda et al. (2012) described the molecular cloud population for clouds identified in the CO(3-2) line emission, with an angular resolution of $1.42\text{arcsec} \times 1.12\text{arcsec}$ based on observations of SMA, and they made no comment about finding two molecular cloud populations. Recent results by Zaragoza-Cardiel et al. (2013) showed two populations of HII regions in another interacting galaxy system Arp 270 which, the authors suggested, are the result of the evolution of two populations of molecular clouds.

In the present paper, we present a comparison of the observed properties of the molecular clouds and HII regions in Arp 244 inferring what this comparison can tell us about the evolution of massive molecular clouds into luminous HII regions. For this purpose, we combined data from the ALMA (Atacama Large Millimeter/submillimeter Array) radio interferometer for the molecular clouds, and the Fabry-Perot optical interferometer GHαFaS (Galaxy Hα Fabry-Perot system) for the HII regions.

In section §2 we present ALMA observations and the GHαFaS observations and data reduction. In section §3 we show how we have estimated the different properties of the HII regions and the GMCs. In section §4 the results relative to the proposed presence of two regimes of star forming regions are shown. In section §5 we give evidence supporting a scenario where the more massive regions are gravitationally bound rather than being bounded by the external pressure. Finally, in section §6 we present our conclusions.

2 OBSERVATIONS

We present two sets of observations of the Antennae: data cubes of emission in Hα from the ionized component of the interstellar medium, and of emission in the CO(3-2) line from the molecular component.

2.1 ALMA observations

We used three different mosaics of the Antennae system from ALMA, covering three zones. The first two mosaics of the observations in the CO(3-2) line are from the ALMA Science Verification programme¹. The third mosaic in the CO(3-2) line is from the ALMA Early Science Cycle 0 archive (project ADS/JAO.ALMA#2011.0.00876.S)². The Science Verification data have been described in Herrera et al. (2012). The Early Science mosaic is derived from a series of observations from 2012 July to November. The total on source time is 3 h with 14 to 24 antennas and baselines from 21 to 402 m.

¹ <http://almascience.eso.org/alma-data/sciver/AntennaeBand7/>

² <http://almascience.eso.org/alma-data/archive>

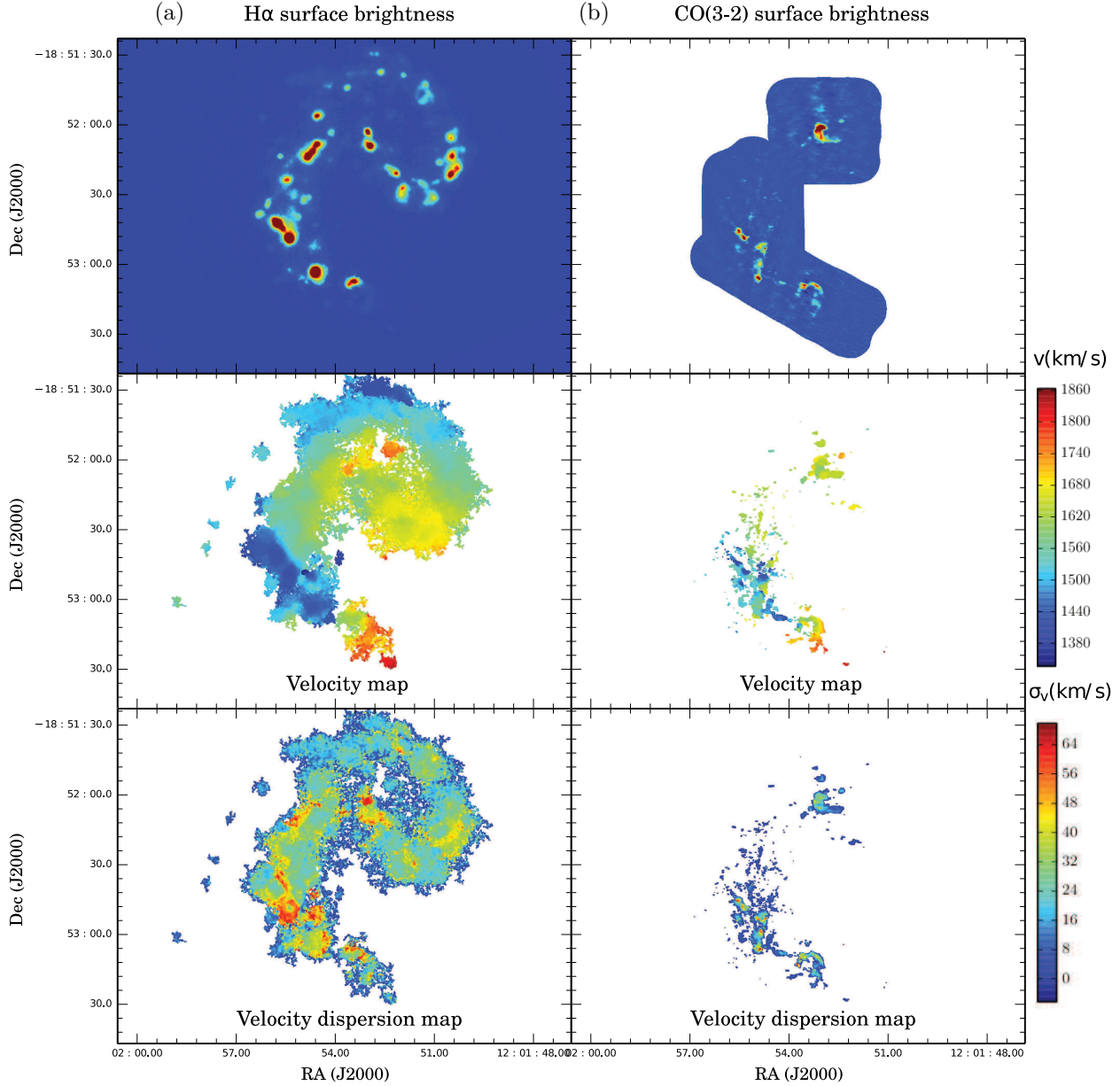


Figure 1. Moment maps of The Antennae galaxies. (a) Derived from the GHαFAS datacube. (b) Derived from the ALMA datacube. The Hα datacube as well as the product moment maps are available through CDS.

We have used the reduced mosaic published in the archive where the raw data have been corrected for atmospheric effects, and flux, bandpass, phase, and amplitude calibrations have been applied. We then corrected the Science Verification and the Early Science mosaics for the primary beam response.

The angular resolution for both mosaics is superior (synthesized beam $\sim 0.6\text{arcsec} \times 1.1\text{arcsec}$ for the Science Verification data, synthesized beam $\sim 0.4\text{arcsec} \times 0.7\text{arcsec}$ for the Early Science data) to those of previous observations (Ueda et al. 2012; Wei et al. 2012). Assuming a distance to the Antennae of 22Mpc (Schweizer et al. 2008), the synthesized beam size $64\text{pc} \times 117\text{pc}$ for the two first mosaics (Science Verification data) and $41\text{pc} \times 61\text{pc}$ for the Early Science,

while the velocity is binned in channels of 10km s^{-1} in both cases. Larger than 420pc structures for Early Science and larger than 354pc structures for Science Verification are not detected due to the lack of short and zero spacing. However, structures of this size or larger are not required for our analysis as we will see below. The ALMA maps covered the areas shown in Fig. 1 (b), where we show the moment maps derived. CO surface brightness is shown as moment 0, (integrated intensity), the velocity map as moment 1 (intensity weighted velocity field), and the velocity dispersion map as moment 2 (intensity weighted velocity dispersion). The velocity and velocity dispersion maps have been masked in order to consider only locations where the line is stronger than a minimum detectable value: $4 \times l_{\text{rms}}$.

The rms in a single channel is $l_{\text{rms}} = 3 \text{ mJy/beam}$ for the Science Verification data and $l_{\text{rms}} = 2 \text{ mJy/beam}$ for the Early Science data with a channel size of 10 km/s in both cases. We have used the three mosaics separately, and in the region where Early Science and Science Verification data overlap, we use Early Science data because of its better sensitivity and resolution. This yields an inhomogeneous data set, and this is why we use a method unbiased with respect to sensitivity and resolution, as described below, to analyse the data.

2.2 GHαFaS observations

Our observations in Hα were taken with the GHαFaS Fabry-Perot interferometer (Hernandez et al. 2008) on the 4.2m William Herschel Telescope (WHT) at the Observatorio del Roque de los Muchachos, La Palma. on the night of 2012 January 24. The seeing limited angular resolution of 0.9 arcsec , 96 pc at the assumed distance of 22 Mpc , was very close to that of the ALMA CO observations, while the velocity resolution, at 8 km s^{-1} is also similar to that in the ALMA observations. The velocity range of the observation is from 1029 to 2211 km/s .

The Hα map, shown in Fig. 1 (a), covered an area on the sky of $3.4 \times 3.4 \text{ arcmin}^2$. For details of the data processing of the Fabry-Perot data we refer the reader to Blasco-Herrera et al. (2010).

A continuum-subtracted and flux-calibrated ACAM (auxiliary-port camera) Hα image was used to perform the flux calibration of the GHαFaS data. ACAM is an instrument mounted permanently at the WHT used for broadband and narrow-band imaging. Fluxes from selected H II regions in both the GHαFaS cube and the ACAM image were measured, and then compared following the procedure explained in Erroz-Ferrer et al. (2012).

Calibrating in velocity and phase adjustment yields a data cube to which we applied the procedures described in Daigle et al. (2006) to derive maps of Arp 244 in Hα surface brightness, velocity and velocity dispersion, which are shown in Fig. 1 (a). The reduced Hα data cube and the derived moment maps are available through CDS. The rms in a single channel is $l_{\text{rms}} = 8 \times 10^{-19} \text{ erg s}^{-1} \text{ cm}^{-2} \text{ Å}^{-1}$ ($1.1 \mu\text{Jy}$) with a channel size of 8 km/s .

3 PROPERTIES OF HII REGIONS AND GMCS

We used DENDROGRAM³, a PYTHON package to compute “dendrograms” of astronomical data (Rosolowsky et al. 2008) to derive the luminosity, radius and velocity dispersion of the HII regions and molecular clouds using the GHαFaS and ALMA datacubes, respectively. To facilitate the reading of this paper we describe briefly how the properties are extracted from the datacubes. For more details we refer the reader to the original sources, Rosolowsky & Leroy (2006); Rosolowsky et al. (2008), of which our description below is a summary.

Both ALMA and GHαFaS datacubes can be described as a collection of values, T_i , at a given 2D spatial point,

(x_i, y_i) , and at a given velocity, v_i . A region is separated from the rest of the cube by an isosurface of value T_{edge} , where $T > T_{\text{edge}}$ inside the region and $T < T_{\text{edge}}$ just outside the region. The major and minor axes of the region are estimated as the mean values of the second spatial moments in the directions of these axes, respectively:

$$\sigma_{\text{maj,min}} = \sqrt{\frac{\sum_i T_i (x_i - \bar{x})^2}{\sum_i T_i}}, \quad (1)$$

where x represents the points lying on the major or the minor axis of the region and the sum is over the pixels inside the region. The radius, assuming a spherical region, is $R = \eta \sqrt{\sigma_{\text{maj}} \sigma_{\text{min}}}$, where $\eta = 1.91$.

The velocity dispersion estimate is the second moment of the velocity axis weighted by the data values

$$\sigma_v = \sqrt{\frac{\sum_i^{\text{region}} T_i (v_i - \bar{v})^2}{\sum_i^{\text{region}} T_i}} \quad (2)$$

where

$$\bar{v} = \frac{\sum_i^{\text{region}} T_i v_i}{\sum_i^{\text{region}} T_i} \quad (3)$$

and the sum is over all the pixels inside the region defined by T_{edge} .

The flux is estimated as the zeroth moment $F = \sum_i T_i \delta v \delta x \delta y$, where δx , δy , and δv are the pixel sizes.

The value of T_{edge} adopted here is $T_{\text{edge}} = 4 \times l_{\text{rms}}$. However, the method is unbiased with respect to T_{edge} . The rms of the datacube is used to set the size of the intervals where the method looks for new clouds. We set this parameter as $4 \times l_{\text{rms}}$, and a minimum pixel area set by the resolution of each observation. Rosolowsky et al. (2008) describe three paradigms for measuring the properties from datacubes, the one used here is the “bijection” paradigm.

3.1 Properties of HII regions

3.1.1 Dust attenuation corrected Hα luminosity

The Antennae have quite heavy and variable attenuation (Brandl et al. 2005), as expected for a system with widespread ongoing massive star formation. This implies that the observed Hα does not take fully into account the HII region population, as the most deeply embedded regions are not observed. We have made the best possible correction for dust extinction and believe that the statistical impact of the missing regions is not crucial. In order to correct for this dust attenuation, we used archival *HST* data of The Antennae galaxies with narrow band filters in Hα F658N, and Hβ F487N. Using the broadband filter F814W (close to I) we subtracted the continuum in the Hα and Hβ images following the procedure described in Gutiérrez et al. (2011). Assuming case B recombination the intrinsic Balmer line ratio is $L_{\text{H}\alpha}/L_{\text{H}\beta} = 2.87$ (Osterbrock 1989), and assuming a value of the attenuation curve estimated from Calzetti et al. (2000) of $K(\text{H}\alpha) = 3.33$ and $K(\text{H}\beta) = 4.60$ we have made an individual correction of the Hα luminosity of each HII region pixel by pixel for dust attenuation in the Antennae. The colour excess is $E(B - V) = 1.38$ around the NGC

³ <http://www.dendrograms.org>

4038 nuclei and $E(B - V) = 0.68$ around the NGC 4039 nuclei. In the rest of the galaxies, except in the overlap region $E(B - V) \in [0, 1]$ while the overlap region between the two galaxies is where the maximum colour excess is measured $E(B - V) \in [0, 1.84]$. These values are representative, and in practice we corrected each pixel individually for extinction.

The results we present here are corrected for this dust attenuation, although the results without this correction are qualitatively similar.

3.1.2 Derived properties of HII regions

Given the dust-corrected H α luminosity, $L_{H\alpha}$, the radius of the HII region, R_{HII} , and the velocity dispersion, σ_v , we can derive a number of physical parameters, e.g. the electron density, n_e , following Relaño et al. (2005) (equation 6), assuming spherical HII regions composed of hydrogen with uniform density (Spitzer 1978)

$$\frac{L_{H\alpha}}{\pi R_{HII}^{cm2}} = h\nu_{H\alpha} \alpha_{H\alpha}^{eff}(H_0, T) 2.46 \cdot 10^{17} \cdot n_e^2 R_{HII}^{cm} \quad (4)$$

where $\alpha_{H\alpha}^{eff}(H_0, T)$ is the effective recombination coefficient of the H α emission line, $h\nu_{H\alpha}$ is the energy of an H α photon, and R_{HII}^{cm} is the radius in cm of the HII region. We implicitly assume that the H α emission is due to photoionization. However, observations have suggested the presence of shocks in the Antenna (Haas et al. 2005; Herrera et al. 2012; Wei et al. 2012). Diagnostics to estimate the amount of photoionization versus ionization by shocks have been made for a few galaxies yielding the result that a rather small fraction of the ionization is due to non-photoionization processes (Calzetti et al. 2004), about 3% – 4%. However the diagnostics have a degree of degeneracy, so that in an extreme case the fraction of ionization by shocks can reach 33% (Hong et al. 2011), although these authors give canonical values of less than 15% in their study. It is necessary to specify here that equation 4 is valid where there is not a significant contribution from ionization by shocks.

Using equation 4, the ionized gas mass (M_{HII}) is given by:

$$M_{HII}(M_\odot) = \frac{4}{3} \pi R_{HII}^3 n_e m_p = 1.57 \times 10^{-17} \sqrt{L_{H\alpha} \times R_{HII}^3} \quad (5)$$

where $m_p = 1.67 \times 10^{-27}$ kg is the proton mass, $L_{H\alpha}$ is in erg/s, and R_{HII} is in pc.

We have subtracted the instrumental, natural and thermal widths in quadrature from the observed velocity dispersion. We estimate a natural width of 3 km/s using the data from Clegg et al. (1999) for the seven fine structure components of H α for an HII region with $N_e \sim 10^2$ and $T \sim 10^4$ K. We consider a thermal width of an isothermal HII region with temperature $T = 10^4$ K of 9.1 km/s (O'dell & Townsley 1988).

Using the non-thermal velocity dispersion and the ionized gas mass, M_{HII} , we can approximate the virial parameter $\alpha_{vir} = 5 \frac{\sigma_v^2 R_{HII}}{GM_{gas}}$ (Bertoldi & McKee 1992) assuming $M_{gas} = M_{HII}$. In an HII region there is more mass involved than the ionized gas. However, the results we will present below comparing properties of HII regions and molecular

clouds, enable us to compare ionized gas with molecular gas mass and conclude that the fraction of ionized gas over total gas mass must be nearly constant. Under these conditions the true values of the virial parameter for the HII regions must be a nearly constant fraction of those estimated here. In practice our estimate of the virial parameter is uncertain by an essentially constant factor due to the non uniform density distributions and deviations from sphericity in clumps (Bertoldi & McKee 1992).

We also derive the star formation rates (SFR) for each HII region using the dust-corrected H α luminosity and the calibration in Kennicutt et al. (2009). Brandl et al. (2009) found $SFR \in [0.2, 2.0] M_\odot/\text{yr}$ in the Antennae for the brightest star forming regions compatible with our SFR estimated for the brightest HII regions $[2.8, 0.8, 0.68, 0.3, \dots] M_\odot/\text{yr}$ (see Table A).

3.2 Properties of molecular clouds

As in Wei et al. (2012), the molecular gas mass was estimated from the CO luminosity following Solomon et al. (1992):

$$\frac{L_{CO}}{\text{K km s}^{-1} \text{ pc}^2} = 3.25 \times 10^7 \left(\frac{\nu_{rest}}{\text{GHz}} \right)^{-2} (1+z)^{-1} \times \left(\frac{D_L}{\text{Mpc}} \right)^2 \left(\frac{F'_{CO}}{\text{Jy km s}^{-1}} \right) \quad (6)$$

where ν_{rest} is the rest frequency of the line (345.796 GHz in the case of CO(3-2)), D_L is the luminosity distance, assumed 22 Mpc along the paper, and F_{CO} is the velocity-integrated flux measured in the datacube. Then, using the relation between CO luminosity and molecular gas mass, $M_{H_2} = \alpha_{CO} L_{CO}$ (where $\alpha_{CO} = 2m_H X_{CO}$), we obtain the molecular gas mass, M_{H_2} , assuming $\alpha_{CO} = 4.8 M_\odot (\text{K km s}^{-1} \text{ pc}^2)^{-1}$, the same value as in Wei et al. (2012) and in Ueda et al. (2012). There is a conflict for the value of α_{CO} in the Antennae, some works claim that the value is a few times smaller than the Galactic value of $\alpha_{CO} = 4.5$ (Zhu et al. 2003; Bolatto et al. 2013) while other studies claim that the value of α_{CO} in the Antennae is close to the Galactic value (Wilson et al. 2003; Schulz et al. 2007). We have chosen the value close to the Galactic value for consistency with Wei et al. (2012), Ueda et al. (2012), and Roman-Duval et al. (2010). We have corrected α_{CO} by a factor of 1.8 since we are using CO(3-2) intensities, and from Ueda et al. (2012) we know that the average ratio $\frac{I_{CO(1-0)}}{I_{CO(3-2)}} \simeq 1.8$ in the Antennae galaxies. Furthermore, we have applied a factor of 1.36 in order to take into account helium and heavier elements in the molecular cloud masses (Allen 1973).

We then went on to estimate the density assuming spherical clouds, ρ_{mol} , and the virial parameter, $\alpha_{vir} = 5 \frac{\sigma_v^2 R}{GM_{gas}}$, assuming $M_{gas} = M_{mol}$ for the molecular clouds.

3.3 Uncertainties

We have followed the procedure (the bootstrapping method) explained in Rosolowsky & Leroy (2006) to derive the errors in the measured properties. This method consists of randomly sampling each region allowing repeated values. The

error is estimated as the standard deviation of the new derived properties scaled up by the square root of the number of pixels in one resolution element in the $H\alpha$ data, and in one beam in the ALMA data. This uncertainty does not include the intrinsic error of the flux in the data cubes.

We show the values of these computed physical parameters for the 303 HII regions in Table A1, and the 142 molecular clouds detected in Table A2. However, as we are resolution limited at the small radius end of the distribution of HII regions and molecular clouds we removed regions with an uncertainty in size greater than 20% except in the comparison of our GMCs with those from Ueda et al. (2012) (Fig. 6) since they do not estimate uncertainties. This comparison would not be complete if we did not consider all GMCs detected in our data. After removing the regions most affected by the noise, the number of HII regions is 201 and the number of GMCs is 89.

4 RESULTS

Fig. 2 (a) shows the mass-radius relation for molecular clouds (blue) compared with data of the Antennae from Ueda et al. (2012) (green). Fig. 2 (b) shows the same relation for HII regions (red). The scales are different because the sizes of HII regions are bigger (as expected since they have been “puffed up” during the ionization and heating process) and our estimates of the HII region masses take into account only the ionized gas mass; for the molecular clouds, we have estimated the molecular gas mass.

The comparison between our data from ALMA and the data from Ueda et al. (2012) using SMA shows that they are compatible, but our results have twice better angular resolution and 24 times better sensitivity enabling us to resolve larger molecular clouds into smaller ones. The results of ALMA cover a wider range of masses and sizes compared with the results of SMA.

Despite the fact that the HII regions have evolved considerably from their original molecular clouds, HII regions and molecular clouds show similar forms for the mass-radius relation (Fig. 2 (a,b)). Furthermore, assuming that a molecular cloud would not be larger than its corresponding evolved HII region, we infer that we are not missing any flux in the molecular clouds due to the lack of the u, v coverage since the largest HII region size is 281 pc.

4.1 Molecular clouds results

In this work, we have found that the exponent N in the mass-radius relation ($M \propto R_{\text{CO}}^N$) is significantly higher than 2, in contrast to the results of previous studies for Galactic molecular clouds, Larson (1981) found $N = 1.9$, Roman-Duval et al. (2010) found $N = 2.36$, Lombardi et al. (2010) found $N = 1.6$, Kauffmann et al. (2010) found $N = 1.33$ and extragalactic GMCs where Colombo et al. (2014) found $N \in [1.5, 2.2]$.

In Fig. 2 (a) we show the linear fit estimated for the molecular clouds (blue). The results of the error weighted fit is:

$$\log(M_{\text{mol}}) = (2.4 \pm 0.4) + (2.62 \pm 0.10) \log(R_{\text{CO}}) \quad (7)$$

where M_{mol} units are M_{\odot} , while R_{CO} units are pc. We note that the exponent is $N = 2.62$ which means that the molecular gas surface density increases with the size, or with the mass of the cloud, in contrast with previous studies where a nearly constant gas surface density is found.

4.2 HII region results

In order to compare molecular clouds and HII region results, we need to convert the $H\alpha$ luminosity-radius relation to the corresponding ionized gas mass-radius relation.

From equation 5 we can infer that if the exponent in the $H\alpha$ luminosity-radius relation ($L_{H\alpha} \propto R_{\text{HII}}^Q$) is $Q < 3$ then the exponent in the ionized gas mass-radius relation ($M_{\text{HII}} \propto R_{\text{HII}}^N$) would also be $N < 3$, and if $Q > 3$, then $N > 3$.

In previous studies of HII regions values of $Q < 3$ were obtained (Terlevich & Melnick 1981; Gutiérrez et al. 2011). However, the most luminous HII regions in Arp 270 had $Q = 3.8$ in the $L_{H\alpha} \propto R_{\text{HII}}^Q$ relation, from results of Zaragoza-Cardiel et al. (2013) differing from the relation shown above found for essentially non-interacting galaxies. Instead of using $H\alpha$ luminosity for HII regions, we use the ionized gas mass derived from equation 5.

Here we have performed a double linear fit to the ionized gas mass-radius relation, keeping as a fit coefficient the transition between one linear fit and another one.

In Fig. 2 (b), the double linear error weighted fit is shown for HII regions (red line). The results of the fit are

$$\log(M_{\text{HII}}) = (1.6 \pm 0.4) + (1.8 \pm 0.3) \log(R_{\text{HII}}); \quad (8)$$

for $\log(R_{\text{HII}}) \leq 1.9$

$$\log(M_{\text{HII}}) = (-1.7 \pm 0.5) + (3.7 \pm 0.2) \log(R_{\text{HII}}); \quad (9)$$

for $\log(R_{\text{HII}}) > 1.9$

where M_{HII} and R_{HII} are in units of M_{\odot} and pc respectively. The transition at $\log(R_{\text{HII}}) = 1.92$ corresponds to a transition at $\log(M_{\text{HII}}) = 5.4$ or using equation 5, a transition at $\log L_{H\alpha} = 38.6$. For the HII regions in the Antennae we see that the less massive regions $\log(M_{\text{HII}}) < 5.4$ follow the trend found in previous work ($N < 3$ in the $M \propto R_{\text{HII}}^N$ relation). For the more massive $\log(M_{\text{HII}}) > 5.4$ regions the slope is higher than 3, implying that the density increases with mass, i. e., the star forming regions are denser as they grow in mass (or in size).

4.3 Density of molecular clouds and HII regions

The change in the mass-size relation is clearly shown in Figure 3 where we show the (ionized) gas density-(ionized) gas mass relation for HII regions and molecular clouds. We plot two scales because, as we explain below, we can make a useful, if somewhat tentative match between the two. In Figure 3, the comparison of the molecular clouds in the Antennae (dark blue) with the molecular clouds in the Milky Way (light blue) shows a decreasing density regime with increasing mass for the Milky Way molecular clouds, while for those in the higher mass range of the Antennae molecular clouds, the density does not decrease with mass. The same pattern occurs for the HII regions in the Antennae comparing them

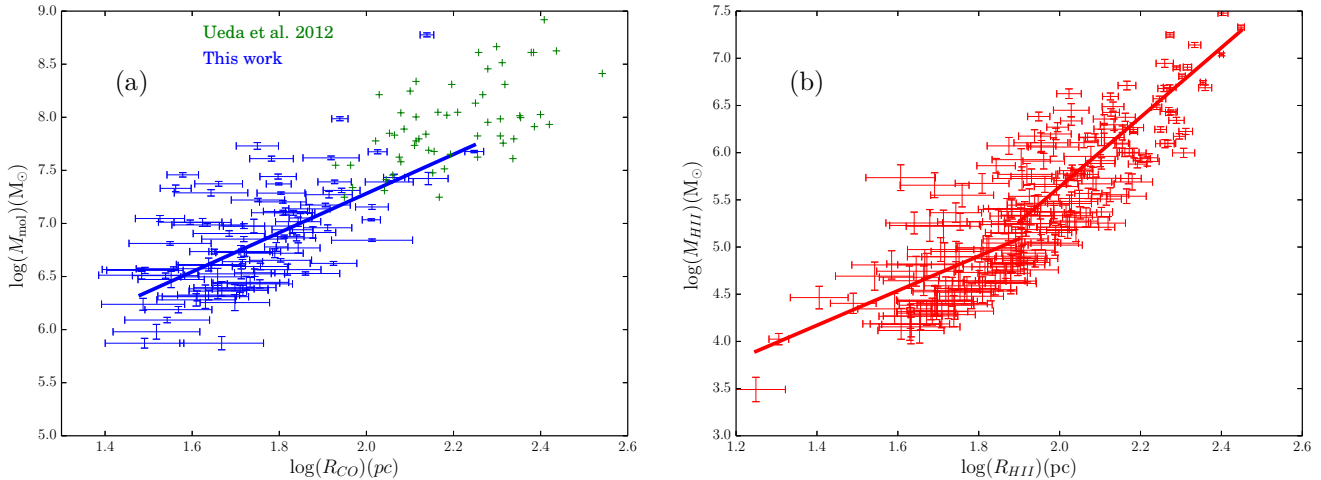


Figure 2. (a) Relation between molecular gas mass, M_{mol} , and molecular cloud size, R_{CO} , for molecular clouds in the Antennae using ALMA data (blue). The blue line is the linear fit result for molecular clouds using ALMA (equation 7). The same relation is plotted for data of the Antennae from Ueda et al. (2012) in green. (b) Relation between ionized gas mass, M_{HII} , and HII region size, R_{HII} , for HII regions in the Antennae using GHαFaS data. The red line is the linear fit result for HII regions (equations 8 and 9)

with Gutiérrez et al. (2011) HII regions for M51. We considered the use, in Figure 3 of the results of Colombo et al. (2014) which we used in section 5, on the molecular clouds of M51. However the lower limit to the cloud masses in Colombo et al. (2014) is only $10^5 M_{\odot}$, and there are very few clouds with masses below $10^6 M_{\odot}$. Using these data, we could not have obtained a useful comparison with the HII regions in M51, where the HST resolution makes the low mass range available. In order to make an indirect comparison we were obliged to use the results of the GMC's in the Milky Way from Roman-Duval et al. (2010). We have seen in the previous section that the transition of mass regimes in the HII regions is at $\sim 10^{5.4} M_{\odot}$ while for the molecular clouds we do not have enough molecular clouds in the lower mass regime in the Antennae, but from Figure 3 it is clear that if we consider the clouds in the Milky Way and the Antennae together we find, at least apparently, a transition compatible with the transition at $\sim 10^{6.5} M_{\odot}$ of the mass function of Wei et al. (2012) and that derived below.

If we adopt a numerical factor which brings into registration the scales for the two types of clouds in the density-mass relation (Figure 3), we can estimate that the expansion factor of a GMC which is transformed into an HII region is ~ 2 , while the ionized gas to total gas fraction is ~ 0.05 as predicted in the models by Giammanco et al. (2004). A more reliable estimate of these two parameters is beyond the scope of this work. An interesting result here is that when we use the ionized gas mass to derive an initial value for the virial parameter, and then go on to find the ionized mass fraction needed to convert the virial parameter to values close to unity in the gravitationally bound regime this fraction is virtually invariant.

We plot the mass function in Fig. 4, which shows the number of regions per mass bin. We find a break in the molecular gas mass function at $\log(M_{\text{mol}}) \sim 6.7$, near the value for which Wei et al. (2012) found a break in the mass function. The evidence for the presence of two populations of molecular clouds is still present in the two populations of HII regions with a break at $\log(M_{\text{HII}}) \sim 5.4$, which corresponds

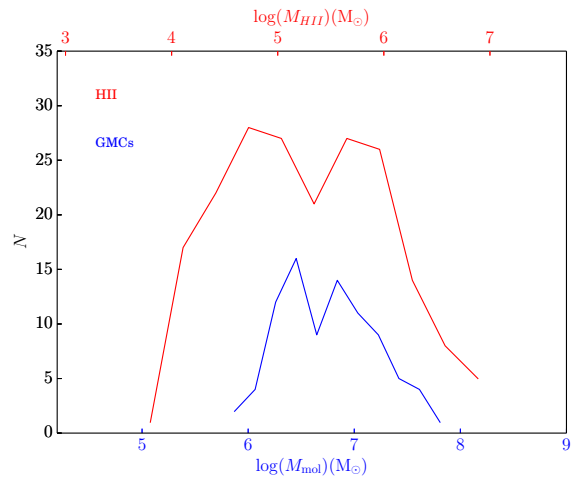


Figure 4. Mass function of molecular clouds (blue) and of HII regions (red) in the Antennae. The blue scale refers to the mass of molecular clouds, M_{mol} , while the red scale refers to the ionized gas mass of the HII regions, M_{HII} .

to a break in the H α luminosity function at $L_{\text{H}\alpha} \sim 38.6\text{dex}$ found with the GHαFaS data. This has also been reported previously in the literature (Kennicutt, Edgar, & Hodge 1989; Bradley et al. 2006). Again, we match the two mass functions using a constant ionized gas fraction around 0.05 as we found previously and as was assumed in the models of Giammanco et al. (2004). The constant ionization fraction gives a match to the break change in the density-mass relation for molecular clouds at $\log(M_{\text{mol}}) \sim 6.7$ and HII regions at $\log(M_{\text{HII}}) \sim 5.4$.

4.4 Location of HII regions and GMCs

In figure 5 we represent the H α surface brightness map, with the HII regions over plotted as white and black circles. There are 80 HII regions in the less massive regime (white circles in

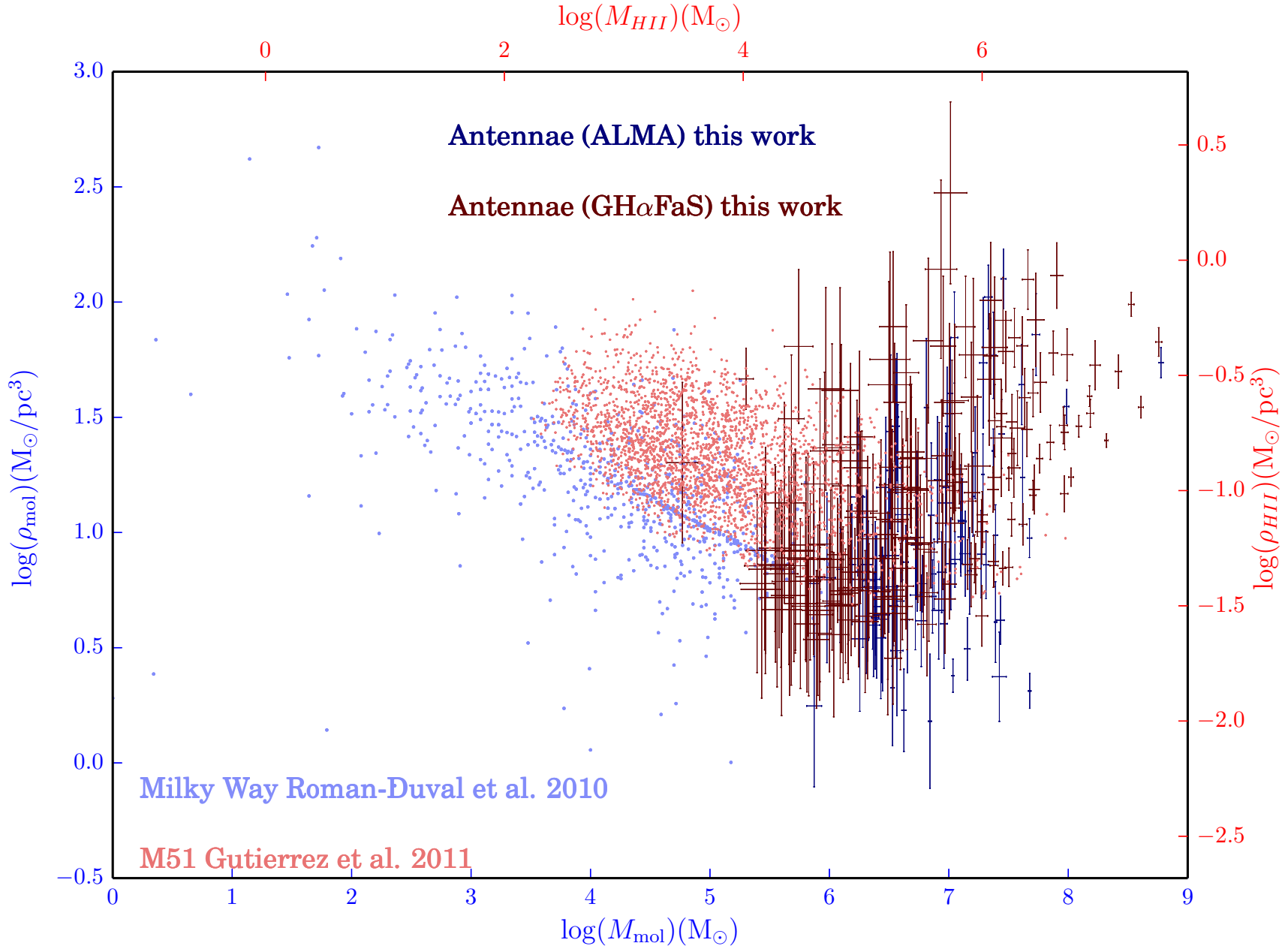


Figure 3. Molecular gas density, ρ_{mol} , versus molecular gas mass of each molecular cloud, M_{mol} , (dark blue). Ionized gas density, ρ_{HII} , versus ionized gas mass for each HII region (dark red), M_{HII} . We show the equivalent data for molecular clouds in the Milky Way data from Roman-Duval et al. (2010) (light blue), and for the HII regions of M51 from Gutiérrez et al. (2011) (light red). The blue scales are for the molecular clouds, and the red scales are for the HII regions.

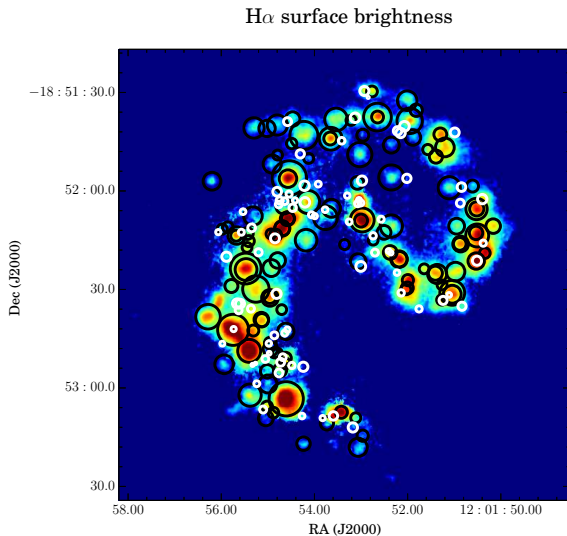


Figure 5. HII regions locations around Antennae galaxies. The intensity colour map is the H α surface brightness derived from the GH α FaS datacube. White circles represent the less massive HII regions ($\log(M_{\text{HII}}) < 5.4$) and black circles represent the more massive HII regions ($\log(M_{\text{HII}}) > 5.4$)

Fig. 5) while there are 121 HII regions in the more massive regime (white circles in Fig. 5). We do not see an obvious correlation between the two regimes and their locations within the galaxies. This result is in contrast with the pattern we found (Zaragoza-Cardiel et al. 2013) in Arp 270 between the two regimes where the regime of the high mass regions was concentrated towards the central part of the galaxies and the overlap region, while regime of the low mass regions was concentrated in the outer parts of the galaxies. We do not see this pattern in the Antennae galaxies almost certainly because they are in a more advanced, and therefore morphologically more complex, stage of the merger process.

In Fig. 6 we show the CO(3-2) surface brightness map with the GMCs represented as black and white circles (56 in the more massive regime, and 86 in the less massive regime respectively). In contrast with the previous sections, we have used the whole sample of GMCs detected independently of the uncertainty in the size of the region as we have explained above. The locations of GMCs is not correlated with the two types of GMCs, as in the case of HII regions. We have plotted, in order to compare, the regions from Ueda et al. (2012) as green circles. In Fig. 6, it is clear that the data of this work compared with the data from Ueda et al. (2012) are improved because of the better spatial coverage, sensitivity, and spatial resolution.

5 GRAVITATIONALLY BOUND REGIME

It is not clear what is the relative importance of the different forces which control the physical behaviour of molecular clouds and HII regions (gravity, magnetic field, external pressure, shear, etc.). It is also notable that environment may play a specific role in the behaviour of star forming regions, and subsequently of star formation. Articles with star formation models, and observations, from Elmegreen & Efremov (1997) and Ashman & Zepf (2001) claim that the external

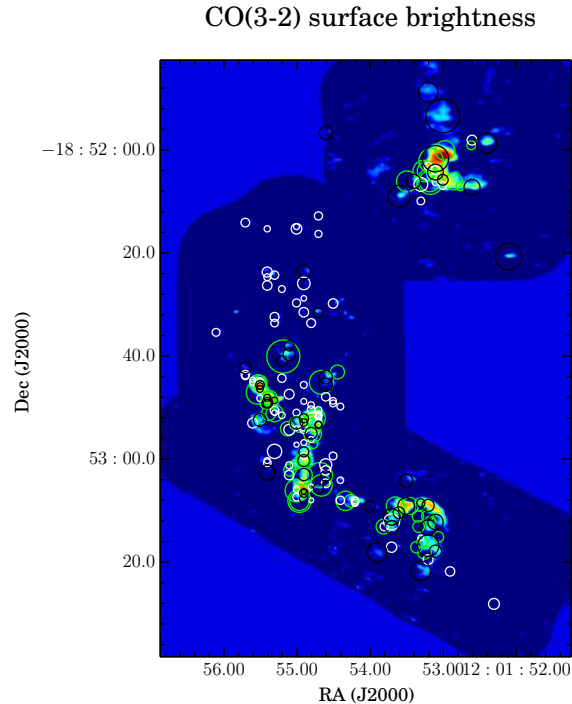


Figure 6. GMC locations around Antennae galaxies. The intensity colour map is the CO(3-2) surface brightness derived from the ALMA datacubes. White circles represent the less massive GMCs ($\log(M_{\text{mol}}) < 6.7$), black circles represent the more massive GMCs ($\log(M_{\text{mol}}) > 6.7$), and green circles represent the GMCs detected by Ueda et al. (2012)

pressure is the driver of the star formation in starburst regions, but that the mass and the self-gravity of the star forming regions should also play a role.

Wei et al. (2012), claimed that the high mass population of molecular clouds is gravitationally bound based on the relation between virial and molecular gas mass. We also note that Gutiérrez et al. (2011) showed clearly that the HII regions in M51 are pressure bounded by the external gas column density, (we note that these are regions with luminosities below 38.6dex) while Zaragoza-Cardiel et al. (2013) claimed that for Arp 270 the brightest HII regions are different in this respect from those in M51 based on their scaling relations, and they concluded that the brightest HII regions are gravitationally dominated while for the fainter HII regions, the dominant force is the external pressure rather than gravity.

The tools we have used in the present study to check this hypothesis are the luminosity-velocity dispersion ($L_{\text{H}\alpha} - \sigma_v$) relation (Relaño et al. 2005) and the virial parameter (Bertoldi & McKee 1992).

The ($L_{\text{H}\alpha} - \sigma_v$) relation for HII regions usually presents an envelope through the brightest regions. For each luminosity, a range of velocity dispersion values is present. The envelope is formed by the regions showing the minimum velocity dispersion for given luminosity (see Fig. 7 (a)). We follow the method of Relaño et al. (2005) to estimate the envelope. They simply selected the HII region with the minimum velocity dispersion for each luminosity bin. Furthermore, they suggested that the envelope in the luminosity-

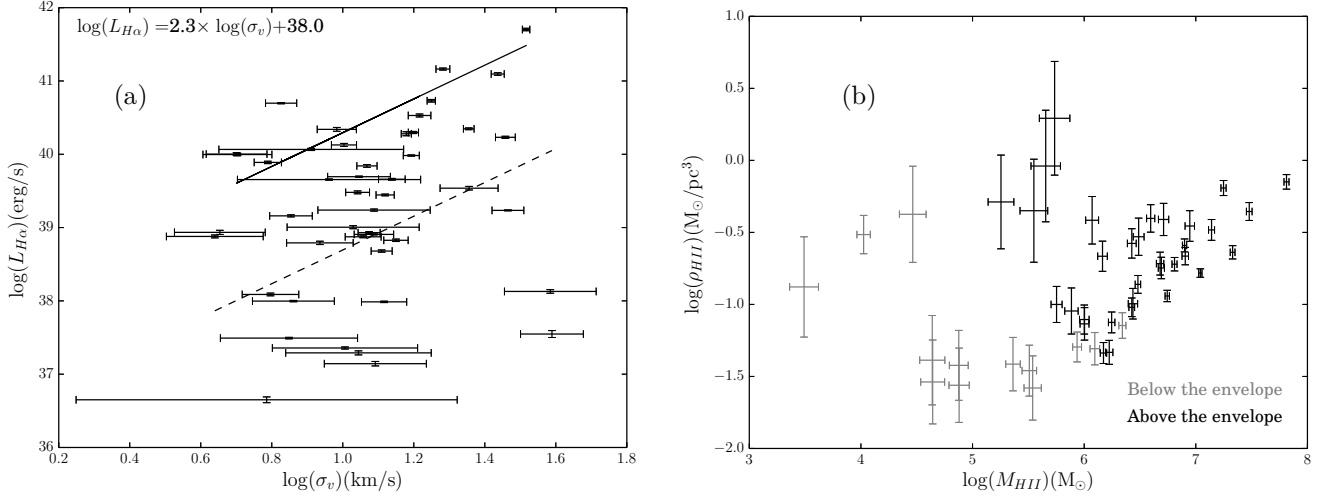


Figure 7. (a) $H\alpha$ luminosity, versus velocity dispersion, σ_v for the HII regions. The thermal, natural and instrumental widths have been subtracted quadratically. The results of the estimates involving the envelope as described here are shown as a solid line. The dashed line is the same estimate, but shifted by a constant value. (b) Ionized gas density, ρ_{HII} , versus ionized gas mass, M_{HII} , of the HII regions. Regions in grey represent those which are below the shifted envelope (dashed line) in Fig. 7 (a). Regions in black represent those which are above the shifted envelope (dashed line) in Fig. 7 (a).

velocity dispersion may be formed by virialized regions i. e. those that are gravitationally dominated.

We have tested this option for the HII regions in the Antennae. (We might also have plotted the equivalent envelope in the $M_{\text{mol}} - \sigma_v$ for the molecular clouds, although for these we do not have a big enough set of the less massive clouds).

The $L_{H\alpha} - \sigma_v$ relation is shown in Fig. 7 (a) for HII regions. We removed HII regions with line widths less than 8km/s, i.e., velocity dispersions less than 4km/s, which is the effective velocity resolution of the instrument (8km/s for GHαFAS).

We have assumed, for simplicity, that the regions lying on the envelope follow a linear relation in the log-log plane

$$\log(L_{H\alpha \text{ env}}) = \beta_1 \times \log(\sigma_v) + \beta_0. \quad (10)$$

The result is $\beta_1 = 2.3$, $\beta_0 = 38.0$, accounting just for the HII regions on the envelope, those with the minimum velocity dispersion per luminosity bin. The fit plotted is shown in Figure 7 (a) as a continuous line. We want to separate the regions that are close to the envelope from those which are not. Thus, for a given $(L_{H\alpha}, \sigma_v)$ values of an HII region, we consider that region is close to the envelope if $L_{H\alpha} > \frac{L_{H\alpha \text{ env}}}{40}$, where $L_{H\alpha \text{ env}}$ is derived from equation 10 using the velocity dispersion of the region. This criterion is represented as a dashed line in Fig. 7 (a). The relation between the gas mass and the gas density is plotted in 7 (b). The regions in this plot are separated as previously explained, grey symbols represent regions below the shifted fit of the envelope, while black symbols represent regions above the shifted envelope. It is clear in Fig. 7 (b) that regions above the shifted envelope belong to the more massive regime where the gas density increases with mass. Regions below the shifted envelope belong to the less massive regime where gas density decreases with mass.

In addition, the $H\alpha$ luminosity of the regions lying on

the unshifted envelope, or as explained above, the regions in the higher luminosity (or more massive) regime, is correlated super-linearly with the velocity dispersion. Thus, the SFR derived from the $H\alpha$ luminosity is correlated with the velocity dispersion for the more massive regions. Although $H\alpha$ is an imperfect measure of the SFR, our values are carefully dust corrected and we believe that further refinement would not change any of the conclusions.

The virial parameter, $\alpha_{vir} = 5 \frac{\sigma_v^2 R}{GM_{\text{gas}}}$, can be used to make a test between a regime dominated by external pressure and a gravitationally dominated regime. $\alpha_{vir} \gg 1$ represent regions confined by external pressure where the self-gravity does not dominate. However, $\alpha_{vir} \simeq 1$ represent regions where the velocity dispersion of the cloud can be accounted for by gravity. In this case, the gravity is the driver of the velocity dispersion and it is the dominant force (Bertoldi & McKee 1992).

We plot the virial parameter versus the gas mass in Fig. 8. The reason why the virial parameter reaches values smaller than 1 in the molecular clouds is due to the effects of nonuniformity in density and deviations from sphericity.

For the HII regions the virial parameter value for the less massive regions is greater than unity as expected if the external pressure is the dominant force. In the more massive HII regions the virial parameter decreases, as expected if gravity becomes dominant as the mass increases, supporting the hypothesis that the difference between regimes is due to different dominant forces. In the case of GMCs we do not detect clouds in the less massive regimes. We have added the GMCs detected in Colombo et al. (2014) for M51 since they estimated the virial parameter. Fig. 8 shows that the virial parameter decreases with molecular gas mass combining GMCs from both data sets, implying that external pressure becomes more important in the less massive regions. However, in the more massive regions the external pressure loses its importance in favour of self-gravity. Although we

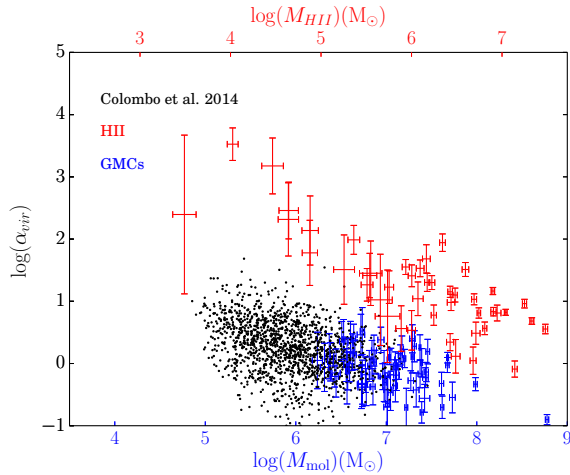


Figure 8. Virial parameter ($\alpha_{vir} = 5 \frac{\sigma_v^2 R}{GM_{gas}}$) versus the ionized gas mass, M_{HII} , for the HII regions (red) and versus molecular gas, M_{mol} , for the molecular clouds in this work (blue) and for M51 (black) from Colombo et al. (2014). In the estimation of the virial parameter, $R = R_{HII}$ for HII regions while $R = R_{CO}$ for the molecular clouds, and $M_{gas} = M_{HII}$ for HII regions while $M_{gas} = M_{mol}$ for molecular clouds.

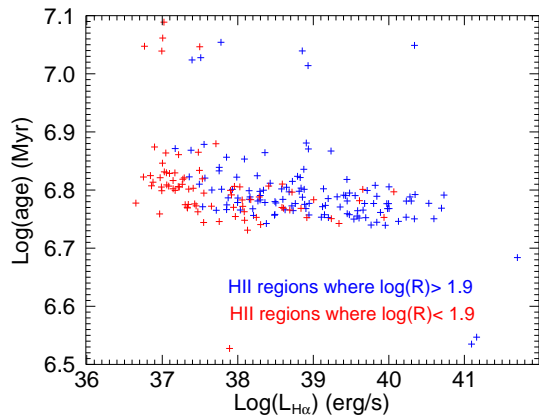


Figure 9. HII region ages derived using the equivalent width and Starburst99 model (Leitherer et al. 1999) versus $H\alpha$ luminosity ($L_{H\alpha}$).

have combined data from two different systems, the result while not conclusive is certainly suggestive.

5.1 Evolutionary processes

Evolution may play a role in the scaling relations of HII regions. However, in Zaragoza-Cardiel et al. (2013) it was shown that the two populations of HII regions in Arp 270 could not be explained, using the $H\alpha$ equivalent width, $W(H\alpha)$, as an effect of age. We can assume a direct relation between $W(H\alpha)$ and the age of the region (Leitherer et al. 1999). The younger the region, the larger is its equivalent width.

We have used the $H\alpha$ map and the continuum map to derive the $H\alpha$ equivalent width. Fig. 9 shows the HII region

ages assuming solar metallicity. We can see that the age ranges for two populations of HII regions are the same. The HII regions are around 6 Myr old. Thus, HII region ages do not play an important role in the scaling relations of the two regimes in the Antennae.

6 CONCLUSION

The scaling relations for the most massive clouds are different from those found for the Milky Way or for non-merging galaxies, where the upper mass limits for these types of objects are lower.

Previous studies show that gas density decreases with mass Roman-Duval et al. (2010); Kauffmann et al. (2010); Gutiérrez et al. (2011). We showed some of these results in Figure 3, where the gas density of the less massive molecular clouds of the Milky Way and the less massive HII regions of M51 decrease with mass.

Furthermore, the properties of the more massive molecular clouds in the Antennae galaxies using archive ALMA data are different from those of the less massive ones. The gas density does not decrease with mass. We have been able to see both regimes in the ionized gas density of the HII regions, one where the ionized gas density increases with ionized mass (for $M_{HII} > 10^{5.4} M_{\odot}$), and another one where the ionized gas density decreases with ionized gas mass (for $M_{HII} < 10^{5.4} M_{\odot}$). The transition is equivalent to the transition found in the mass function of molecular clouds at $M_{mol} = 10^{6.7} M_{\odot}$ in this work and in Wei et al. (2012) if we consider a constant ionization fraction of 0.05, consistent with results found in this work and with models of Giammanco et al. (2004).

In the more massive regime, the more massive the regions are the denser they become. As the SFR does not appear to be linear with the gas density (Schmidt 1959; Kennicutt 1998), the SFR may well be preferentially triggered in these, the most massive clouds.

We have found that there are HII regions where the $H\alpha$ luminosity is correlated with the velocity dispersion. This means that the SFR derived from $H\alpha$ luminosity varies approximately with the square of the velocity dispersion, implying that the regions on the envelope of the luminosity-velocity dispersion relation are probably gravitationally dominated, and this is suggested also by the present study. Moreover, the HII regions on the envelope are those where the gas density increases with mass, while for the HII regions far from the envelope the gas density decreases with mass.

The virial parameter decreases with increasing gas mass implying that gravity rather than external pressure is more dominant for the more massive HII regions and quite probably for the GMCs, but the situation is reversed in the less massive regions, which offers an explanation for why the most massive clouds, be they molecular clouds or HII regions, tend to be denser with increasing mass.

ACKNOWLEDGEMENTS

We thank Johan H. Knapen for allowing us to use observing time with GHaFaS. Based on observations made with

the William Herschel Telescope operated on the island of La Palma by the Isaac Newton Group of Telescopes in the Spanish Observatorio del Roque de los Muchachos of the Instituto de Astrofísica de Canarias. This research has been supported by the Spanish Ministry of Economy and Competitiveness (MINECO) under the grants AYA2007-67625-CO2-01, AYA2009-12903 and AYA2012-39408-CO2-02. JEB acknowledges financial support to the DAGAL network from the People Programme (Marie Curie Actions) of the European Union's Seventh Framework Programme FP7/2007-2013/ under REA grant agreement number PITN-GA-2011-289313.

This research made use of *ASTROPY*, a community-developed core *textscipython* package for astronomy (Astropy Collaboration et al. 2013), *APLPY*, an open-source plotting package for *textscipython* hosted at <http://aplp.github.com>, and *ASTRODENDRO*, a *textscipython* package to compute dendrograms of Astronomical data (<http://www.dendrograms.org/>). The Atacama Large Millimeter/submillimeter Array (ALMA), an international astronomy facility, is a partnership of Europe, North America and East Asia in cooperation with the Republic of Chile. This paper makes use of the following ALMA data:

ADS/JAO.ALMA#2011.0.00003.SV

ADS/JAO.ALMA#2011.0.00876.S

Based on observations made with the NASA/ESA Hubble Space Telescope, obtained from the data archive at the Space Telescope Science Institute. STScI is operated by the Association of Universities for Research in Astronomy, Inc. under NASA contract NAS 5-26555.

We thank the anonymous referee, whose comments have led to important improvements on the original version of the paper.

REFERENCES

- Allen, C. W. 1973, London: University of London, Athlone Press, —c1973, 3rd ed.,
- Anders, P., Bissantz, N., Boysen, L., de Grijs, R., & Fritze-v. Alvensleben, U. 2007, *MNRAS*, 377, 91
- Ashman, K. M., & Zepf, S. E. 2001, *AJ*, 122, 1888
- Astropy Collaboration, Robitaille, T. P., Tollerud, E. J., et al. 2013, *A&A*, 558, A33
- Bertoldi, F., & McKee, C. F. 1992, *ApJ*, 395, 140
- Blasco-Herrera, J., Fathi, K., Beckman, J., et al. 2010, *MNRAS*, 407, 2519
- Bolatto A. D., Leroy A. K., Rosolowsky E., Walter F., Blitz L., 2008, *ApJ*, 686, 948
- Bolatto, A. D., Wolfire, M., & Leroy, A. K. 2013, *ARAA*, 51, 207
- Bournaud F., 2011, *EAS*, 51, 107
- Bradley T. R., Knapen J. H., Beckman J. E., Folkes S. L., 2006, *A&A*, 459, L13
- Brandl, B. R., Clark, D. M., Eikenberry, S. S., et al. 2005, *ApJ*, 635, 280
- Brandl, B. R., Snijders, L., den Brok, M., et al. 2009, *ApJ*, 699, 1982
- Calzetti, D., Armus, L., Bohlin, R. C., et al. 2000, *ApJ*, 533, 682
- Calzetti, D., Harris, J., Gallagher, J. S., III, et al. 2004, *AJ*, 127, 1405
- Chávez, R., Terlevich, R., Terlevich, E., et al. 2014, *arXiv:1405.4010*
- Clegg, R. E. S., Miller, S., Storey, P. J., & Kisieliuss, R. 1999, *A&AS*, 135, 359
- Colombo, D., Hughes, A., Schinnerer, E., et al. 2014, *ApJ*, 784, 3
- Daigle, O., Carignan, C., Hernandez, O., Chemin, L., & Amram, P. 2006, *MNRAS*, 368, 1016
- Dale, J. E., Ercolano, B., & Bonnell, I. A. 2012, *MNRAS*, 424, 377
- Elmegreen, B. G., & Efremov, Y. N. 1997, *ApJ*, 480, 235
- Erroz-Ferrer, S., Knapen, J. H., Font, J., et al. 2012, *MNRAS*, 427, 2938
- Giammanco, C., Beckman, J. E., Zurita, A., & Relaño, M. 2004, *A&A*, 424, 877
- Gutiérrez, L., Beckman, J. E., & Buenroostro, V. 2011, *AJ*, 141, 113
- Haas, M., Chini, R., & Klaas, U. 2005, *A&A*, 433, L17
- Hernandez, O., Fathi, K., Carignan, C., et al. 2008, *PASP*, 120, 665
- Herrera, C. N., Boulanger, F., Nesvadba, N. P. H., & Falgarone, E. 2012, *A&A*, 538, L9
- Heyer, M., Krawczyk, C., Duval, J., & Jackson, J. M. 2009, *ApJ*, 699, 1092
- Hong, S., Calzetti, D., Dopita, M. A., et al. 2011, *ApJ*, 731, 45
- Kauffmann, J., Pillai, T., Shetty, R., Myers, P. C., & Goodman, A. A. 2010, *ApJ*, 716, 433
- Kennicutt R. C., Jr., Edgar B. K., Hodge P. W., 1989, *ApJ*, 337, 761
- Kennicutt, R. C., Jr. 1998, *ApJ*, 498, 541
- Kennicutt, R. C., Jr., Hao, C.-N., Calzetti, D., et al. 2009, *ApJ*, 703, 1672
- Klessen, R. S. 2011, *EAS Publications Series*, 51, 133
- Larson R. B., 1981, *MNRAS*, 194, 809
- Leitherer C., et al., 1999, *ApJS*, 123, 3
- Lombardi, M., Alves, J., & Lada, C. J. 2010, *A&A*, 519, L7
- McKee, C. F., & Ostriker, E. C. 2007, *ARAA*, 45, 565
- Melnick, J., Moles, M., Terlevich, R., & Garcia-Pelayo, J.-M. 1987, *MNRAS*, 226, 849
- Mirabel, I. F., Vigroux, L., Charmandaris, V., et al. 1998, *A&A*, 333, L1
- Moiseev, A. V., Tikhonov, A. V., & Klypin, A. 2014, *arXiv:1405.5731*
- O'dell, C. R., & Townsley, L. K. 1988, *A&A*, 198, 283
- Osterbrock, D. E. 1989, Research supported by the University of California, John Simon Guggenheim Memorial Foundation, University of Minnesota, et al. Mill Valley, CA, University Science Books, 1989, 422 p.,
- Relaño, M., Beckman, J. E., Zurita, A., Rozas, M., & Giammanco, C. 2005, *A&A*, 431, 235
- Roman-Duval, J., Jackson, J. M., Heyer, M., Rathborne, J., & Simon, R. 2010, *ApJ*, 723, 492
- Rosolowsky, E., & Leroy, A. 2006, *PASP*, 118, 590
- Rosolowsky, E. W., Pineda, J. E., Kauffmann, J., & Goodman, A. A. 2008, *ApJ*, 679, 1338
- Sanders, D. B., Mazzarella, J. M., Kim, D.-C., Surace, J. A., & Soifer, B. T. 2003, *AJ*, 126, 1607
- Schmidt, M. 1959, *ApJ*, 129, 243

- Schulz, A., Henkel, C., Muters, D., et al. 2007, A&A, 466, 467
- Schweizer F., et al., 2008, AJ, 136, 1482
- Scoville, N. Z. 2012, arXiv:1210.6990
- Solomon, P. M., Downes, D., & Radford, S. J. E. 1992, ApJL, 398, L29
- Spitzer L., 1978, ppim.book,
- Terlevich, R., & Melnick, J. 1981, MNRAS, 195, 839
- Ueda, J., Iono, D., Petitpas, G., et al. 2012, ApJ, 745, 65
- Wang, Z., Fazio, G. G., Ashby, M. L. N., et al. 2004, ApJS, 154, 193
- Wei, L. H., Keto, E., & Ho, L. C. 2012, ApJ, 750, 136
- Whitmore, B. C., Chandar, R., Schweizer, F., et al. 2010, AJ, 140, 75
- Wilson, C. D., Scoville, N., Madden, S. C., & Charman-daris, V. 2003, ApJ, 599, 1049
- Zaragoza-Cardiel, J., Font-Serra, J., Beckman, J. E., et al. 2013, MNRAS, 432, 998
- Zhu, M., Seaquist, E. R., & Kuno, N. 2003, ApJ, 588, 243

APPENDIX A: PROPERTIES OF THE HII REGIONS AND THE GMC'S

Table A1. Physical properties of the brightest HII regions derived as described in section §3. The whole table is available as a machine readable table in the electronic version of the paper and through CDS.

| N | RA hh:mm:ss | Dec ° / ' / '' | $\log(L_{H\alpha})$ erg/s | SFR M_{\odot}/yr | R_{HII} pc | $\log(M_{\text{HII}})$ M_{\odot} | ρ_{HII} M_{\odot}/pc^3 | σ_v km/s | α_{vir} |
|----|----------------|-------------------|------------------------------|------------------------------|------------------------|---------------------------------------|--|--------------------|-----------------------|
| 1 | 12: 1:55.6 | -18:52:52.0 | 41.7 ± 0.03 | 2.8 | 280 ± 5 | 7.81 ± 0.05 | 0.71 ± 0.03 | 32.8 ± 0.7 | 5.4 ± 0.6 |
| 2 | 12: 1:53.9 | -18:52:42.7 | 41.16 ± 0.03 | 0.8 | 253 ± 6 | 7.48 ± 0.05 | 0.44 ± 0.02 | 19.1 ± 0.7 | 3.6 ± 0.5 |
| 3 | 12: 1:50.9 | -18:52:24.7 | 41.1 ± 0.03 | 0.68 | 187 ± 4 | 7.25 ± 0.05 | 0.64 ± 0.03 | 27 ± 1 | 9 ± 1 |
| 4 | 12: 1:51.2 | -18:52:33.1 | 40.73 ± 0.04 | 0.3 | 281 ± 5 | 7.33 ± 0.04 | 0.23 ± 0.01 | 17.7 ± 0.4 | 4.8 ± 0.5 |
| 5 | 12: 1:53.2 | -18:53: 4.3 | 40.35 ± 0.02 | 0.12 | 195 ± 3 | 6.9 ± 0.04 | 0.26 ± 0.01 | 22.6 ± 0.7 | 15 ± 2 |
| 6 | 12: 1:55.3 | -18:52:52.8 | 40.3 ± 0.03 | 0.11 | 251 ± 2 | 7.04 ± 0.03 | 0.165 ± 0.005 | 15.8 ± 0.5 | 6.6 ± 0.6 |
| 7 | 12: 1:55.3 | -18:52:52.4 | 39.98 ± 0.02 | 0.053 | 187 ± 6 | 6.69 ± 0.06 | 0.18 ± 0.01 | 15.6 ± 0.7 | 11 ± 2 |
| 8 | 12: 1:51.4 | -18:52:25.1 | 39.84 ± 0.04 | 0.038 | 226 ± 3 | 6.74 ± 0.04 | 0.114 ± 0.004 | 11.7 ± 0.7 | 6 ± 1 |
| 9 | 12: 1:54.1 | -18:52: 2.7 | 39.89 ± 0.03 | 0.043 | 134 ± 6 | 6.43 ± 0.08 | 0.27 ± 0.02 | 6.1 ± 0.5 | 2.2 ± 0.6 |
| 10 | 12: 1:51.0 | -18:52:30.8 | 40.13 ± 0.04 | 0.074 | 201 ± 3 | 6.81 ± 0.05 | 0.19 ± 0.009 | 10.1 ± 0.7 | 3.7 ± 0.7 |

Table A2. Physical properties of the brightest molecular clouds derived as described in section §3. The whole table is available as a machine readable table in the electronic version of the paper and through CDS.

| N | RA (hh:mm:ss) | Dec (° / ' / '') | $\log(L_{\text{CO}})$ $\text{K km s}^{-1} \text{ pc}^2$ | R_{CO} (pc) | $\log(M_{\text{mol}})$ M_{\odot} | ρ_{mol} M_{\odot}/pc^3 | σ_v km/s | α_{vir} |
|----|------------------|---------------------|--|-------------------------|---------------------------------------|--|--------------------|-----------------------|
| 1 | 12: 1:53.1 | -18:52: 1.6 | 7.71 ± 0.04 | 138 ± 4 | 8.78 ± 0.04 | 55 ± 7 | 22 ± 1 | 0.13 ± 0.02 |
| 2 | 12: 1:53.5 | -18:53: 9.0 | 6.92 ± 0.04 | 87 ± 3 | 7.99 ± 0.04 | 35 ± 5 | 21 ± 1 | 0.5 ± 0.1 |
| 3 | 12: 1:55.4 | -18:52:49.0 | 6.66 ± 0.06 | 56 ± 5 | 7.73 ± 0.06 | 70 ± 30 | 15 ± 3 | 0.3 ± 0.1 |
| 4 | 12: 1:53.0 | -18:51:53.3 | 6.61 ± 0.02 | 177 ± 8 | 7.68 ± 0.02 | 2.1 ± 0.3 | 16.9 ± 0.9 | 1.2 ± 0.2 |
| 5 | 12: 1:52.4 | -18:51:58.6 | 6.61 ± 0.04 | 106 ± 5 | 7.68 ± 0.04 | 9 ± 2 | 19 ± 2 | 0.9 ± 0.2 |
| 6 | 12: 1:53.1 | -18:52: 4.2 | 6.55 ± 0.04 | 80 ± 10 | 7.62 ± 0.04 | 17 ± 7 | 9.2 ± 0.9 | 0.2 ± 0.07 |
| 7 | 12: 1:53.6 | -18:53:10.3 | 6.54 ± 0.05 | 61 ± 6 | 7.61 ± 0.05 | 40 ± 20 | 17 ± 2 | 0.5 ± 0.2 |
| 8 | 12: 1:54.7 | -18:52:53.3 | 6.39 ± 0.04 | 38 ± 3 | 7.46 ± 0.04 | 130 ± 30 | 32 ± 4 | 1.6 ± 0.6 |
| 9 | 12: 1:54.8 | -18:52:54.9 | 6.37 ± 0.05 | 63 ± 5 | 7.44 ± 0.05 | 27 ± 8 | 17 ± 1 | 0.7 ± 0.2 |
| 10 | 12: 1:53.6 | -18:52: 8.9 | 6.36 ± 0.06 | 116 ± 6 | 7.43 ± 0.06 | 4.2 ± 0.9 | 11 ± 1 | 0.6 ± 0.2 |